Cement and Concrete Composites 133 (2022) 104704

Contents lists available at ScienceDirect

Cement and Concrete Composites

journal homepage: www.elsevier.com/locate/cemconcomp

Time-dependent fresh properties characterization of 3D printing engineered cementitious composites (3DP-ECC): On the evaluation of buildability

Wen Zhou [a], Wes McGee [b], He Zhu [a], H. Süleyman Gökçe [a,c], Victor C. Li [a,*]

[a] Department of Civil and Environmental Engineering, University of Michigan, Ann Arbor, MI, 48109, USA
[b] Taubman College of Architecture and Urban Planning, University of Michigan, Ann Arbor, MI, 48109, USA
[c] Department of Civil Engineering, Bayburt University, Bayburt, 69010, Turkey

ARTICLE INFO

Keywords:
3D printing engineered cementitious composites (3DP-ECC)
Fresh properties
Buildability
Time-dependent model
Self-buckling

ABSTRACT

Failure of the structure due to poor buildability is a major concern in 3D printing of cementitious materials. Evaluation of buildability based on fresh material properties and print parameters is of significance. In this paper, the buildability of printable engineered cementitious composites was investigated and quantified at the material and the structural scale. Fresh ECC material showed excellent load capacity and deformation resistance at the material scale, therefore preventing material failure of the bottom layers, as confirmed by constant shear rate tests and incremental loading tests. To predict vertical deformation of a 3DP structure, a time-dependent strain-stress model of printable ECC was proposed and validated based on the green strength evolution of the material and the buildup rate of the designed structure. At the structural scale, the approach of predicting critical height at self-buckling failure based on stiffness evolution was validated by printing a straight wall and a cylinder structure.

1. Introduction

Extrusion-based 3D printing (3DP) of cementitious material has revolutionized the traditional construction practices and brings new horizons for the development of the construction sector [1–4]. As an automated process, 3D printing transcends the traditional construction mode, showing distinct superiorities in enabling complex geometries, promoting construction efficiency, eliminating formwork, reducing labor, and suppressing environmental impact of construction industry [1,5,6].

3DP imposes complex and sometimes conflicting requirements on the fresh properties of the printed materials, especially at different stages of printing [7–10]. On one hand, the initial fluidity of the cementitious material should be adequate to pump the fresh mixture into the extrusion system before printing. On the other hand, the cementitious material should have a sufficient rigidity to fully bear its own weight once extruded with no further support by the nozzle. Subsequently, as the printed layers stack on the top of each other, the time-dependent increase of stiffness and strength must provide suitable buildability.

Buildability is generally characterized as the ability of the printable material to build up without significant deformation or collapse [8,11,12]. Lack of buildability severely undermines the stability and reliability of the printed element. Generally, failures induced by insufficient buildability fall into two categories: local failure of material and overall collapse of structure [13] (Fig. 1).

At the material scale, the extruded filament must be able to withstand its self-weight and the increasing weight of the gradually built-up superstructure. Therefore, rapid increase of the strength and stiffness capacity is necessary once the filament is in place [8,14–16]. Moderate and controllable deformation under loads facilitates the newly printed filament to join with the previous layer in order to obtain sufficient layer adhesion [3]. Excessive deformation, however, threatens the stability of the structure and results in overall failure. Once the generated vertical stress in the filament exceeds its capacity, the filament will yield or deform significantly, resulting in variation in its cross-sectional shape and instability of the structure.

At the structural scale, even if the stress in a single layer is kept below

* Corresponding author.
E-mail addresses: wzhoucee@umich.edu (W. Zhou), wesmcgee@umich.edu (W. McGee), zhuhe@umich.edu (H. Zhu), hgokce@umich.edu (H.S. Gökçe), vcli@umich.edu (V.C. Li).

https://doi.org/10.1016/j.cemconcomp.2022.104704
Received 22 May 2022; Received in revised form 11 July 2022; Accepted 26 July 2022
Available online 1 August 2022

the stress threshold, without causing any material failure, the cumulative strain and stress accounting for all the layers may impair the shape control and structural stability of the printed object, resulting in overall collapse of the element, especially when the printed structure is slender and vulnerable to self-buckling [3,8,17–19]. To evaluate the structural failure, Suiker [20] suggested mechanical models that consider elastic buckling failure for printed structures. Roussel [8] illustrated the requirements on the material elastic modulus based on the critical height H_c, at which self-buckling is expected to occur in a slender structure, as shown in Eq. (1), to direct the design of materials.

$$H_c \approx \left(\frac{8EI}{\rho g A}\right)^{1/3} \tag{1}$$

where E is the elastic modulus of the fresh material, I is the moment of inertia, ρ is the density of printable material, g is the acceleration of gravity, and A is the horizontal cross-sectional area.

Various approaches have been proposed to experimentally evaluate buildability. The most straightforward one is to compare the maximum height or number of layers that can be stacked under the same print settings [12,21–26]. Nonetheless, to visually inspect the buildability of material, printing is needed for each assessment. This evaluation method is suitable as an indicator for comparative and qualitative studies after printing without providing an effective prediction of buildability. Similarly, vertical strain or deformation of printed element also serves as an indirect evaluation index in post-hoc analysis [27–29]. Another strategy is to predict the buildability of materials in the 3DP process ex ante by measuring material properties. Some of the commonly used material performance indicators include green strength [17,30–35], yield stress [36–39], penetration resistance [38,40] of wet material, etc. It is also suggested that cylinder stability test, which describes the deformation of a concrete cylinder after dynamic tamping or under static loading, can be applied to assess the shape stability of printed material [22]. Nonetheless, these indicators are mostly valued as references at discrete time points and assessed independently with printing parameters. Few studies have combined and interrelated the material evolution and structural buildup on a continuous timeline [16]. Furthermore, the majority of previous studies focus on predicting the critical failure height/layer number. While another concern about 3D printed structure, that of how to estimate and predict the deformation of printed structure when neither material nor structural failure happens, is barely addressed. Panda et al. [32] proposed an approach to estimate the deformation of printed structure based on material stiffness and geometrical parameters. However, the model assumed time-invariant material stiffness, which is only appropriate for evaluation of 3D printing finished within a short printing duration.

In this paper, the focus on buildability evaluation is specifically placed on the 3D printing of engineered cementitious composite (3DP-ECC). As a promising printing ink, engineered cementitious composite (ECC) exhibits robust tensile ductility [41]. Instead of common tension-softening behavior for concrete materials, ECC undergoes strain-hardening and continues to bear higher loads at increasing imposed strain. The growing tensile deformation in ECC is not localized but spreads to multiple microcracks covering an enlarging specimen volume. The multiple microcracking process represents a volumetric inelastic strain deformation analogous to plastic yielding of a ductile metal. This self-reinforcing feature of ECC removes the dependence on steel reinforcement, making ECC an attractive ink for 3D printing.

To date, successful experiences have been gained in printing ECC components [42,43]. Discrepancy in buildability of 3DP-ECC, however, requires more attention. 3D printing of a twisted hollow ECC column up to 1.5 m high has been reported in Ref. [44]. In contrast, ECC elements were reported [45,46] to collapse at less than 17 layers during printing. In addition, 3DP-ECCs with enhanced buildability through optimizing static yield stress [47] and particle size distribution [48] supported the buildup of 120 mm and 210 mm high wall elements, respectively. Such discrepancy stems from the different printing mixture compositions, structural forms, printing setups and parameters. Multiple influencing factors and their interaction prohibit the establishment of a consistent methodology for evaluating the buildability of 3DP-ECC.

To fill the knowledge gap highlighted above, this research aims at providing a quantitative methodology for evaluating the buildability of printable ECC at both the material and the structural scale. At the material scale, constant shear rate tests and incremental loading tests were conducted to assess the material capacity of fresh printable ECC. Further, the green strength of fresh ECC at different ages was characterized to derive a time-dependent strain-stress model, incorporating the influence of print settings (structure buildup rate). At the structural scale, the stiffness evolution of fresh ECC material was analyzed to facilitate the prediction of critical self-buckling height.

2. Experimental programs

2.1. Materials

The binders used include ordinary Portland cement (Type I, Lafarge-Holcim) and fly ash (Class F, Boral Resources), the chemical compositions of which are listed in Table 1 [43]. Silica sand (F75, US Silica) was adopted as fine aggregate. Superplasticizer used in this research (ADVA 198) was a polycarboxylate-based high-range water reducer. Polyvinyl

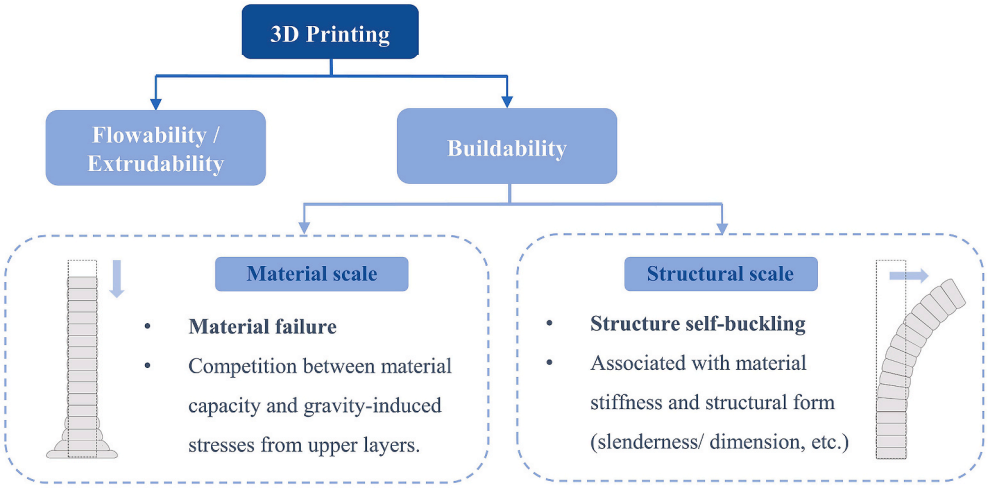

Fig. 1. Failure modes during 3D printing.

Table 1
Chemical compositions of OPC and FA (wt. %).

Material	CaO	Al_2O_3	SiO_2	SO_3	Fe_2O_3	MgO	Others
OPC	63.5	4.8	19.6	2.6	2.9	2.2	4.4
FA	17.4	19.8	39.4	1.9	11.0	3.7	6.8

Note: OPC: ordinary Portland cement; FA: fly ash.

alcohol (PVA) fibers with a length of 8 mm were employed as reinforcement of ECC. The properties of micro PVA fibers are listed in Table 2.

The mix proportions of printable PVA-ECC are shown in Table 3. The water-to-binder ratio and sand-to-binder ratio are 0.24 and 0.29, respectively. The dosage of PVA fiber is 1.5% by volume of the total composition. The bulk density of material is 1984 kg/m^3. For 3D printing, the fresh mixture of PVA-ECC was transferred directly from the mixer to the material hopper at the time of 20 min after water addition. The initial and final setting time of the printable ECC are 110 min and 515 min, respectively.

2.2. Printing setup

The 3D printing system shown in Fig. 2 consists of three main parts. Fresh ECC material is fed into the hopper which is connected to a peristaltic pump system, and then transported through a 15 ft hose to the printing tool. At the inlet position of the printing tool, a pressure sensor is mounted to detect the pressure fluctuation of material flow, and feed the signal back to the peristaltic pump to realize real-time monitoring and adjustment of the pressure. After pumped into the printing tool, fresh material is extruded from a nozzle by a built-in progressive cavity pump inside the tool. The precise positioning and controlling of the printing head are fulfilled by a 6-axis KUKA robot.

2.3. Constant shear rate test

Constant shear rate (CSR) test was conducted to assess the static yield stress evolution of printable ECC. The test applies a quasi-static rotational velocity (commonly 0.1–0.001 s^{-1} [27,36,38,39]) to promote flow onset. A 4-blade vane rheometer (ICAR PLUS concrete rheometer, shown in Fig. 3a) was adopted for the test, with a vane radius of 63.5 mm, a vane height of 127 mm and a container radius of 143 mm. The test started at 20 min after water addition, and the testing protocol was shown in Fig. 3b: (1) pre-shear the fresh mixture at 0.5 s^{-1} for 60 s; (2) rest for 120 s; (3) shear at a constant rate of 0.01 s^{-1} for 60 s; (4) take out the vane, rest the material and repeat (1)–(3) every 20 min. The peak stress measured during each constant rate shear (flow onset) was recorded as the static yield stress of the material.

2.4. Incremental loading test

The layer-by-layer deposition process during printing can be depicted by a stepwise loading process for the underlying material [16]. As each layer of material is deposited, the cumulative compressive load on the underlying material increases accordingly. For example, in this research, the thickness h_0 of each layer is 10 mm, and the corresponding increase in compressive stress can be calculated from Eq. (2).

$$\Delta\sigma_0 = \rho g h_0 \tag{2}$$

where $\Delta\sigma_0$ represents the compressive stress increment, ρ is the density of fresh ECC material, g is the acceleration of gravity.

Table 3
Mix proportions of printable PVA-ECC (Unit: kg/m^3).

OPC	FA	Sand	Water	SP	PVA Fiber
605	678	372	308	1.8	19.5

Note: SP: superplasticizer.

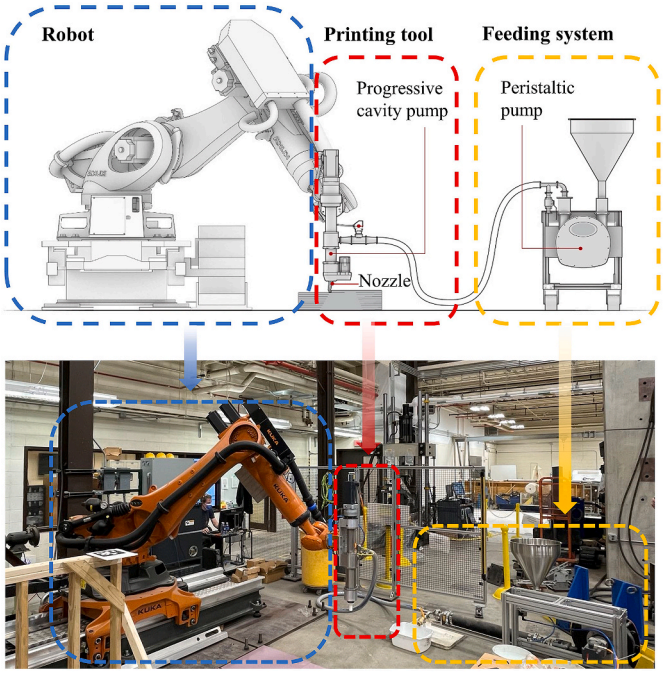

Fig. 2. Printing setups.

For the bottom material with a 50 mm by 50 mm horizontal area, each deposition results in a pressure increase of approximately 0.5 N. As the pressure rises, the stiffness and load-carrying capacity of the fresh material grows simultaneously. The strain and failure of the material under these two competing effects are thus of interest.

To simulate the evolution of the upper layer load, fresh ECC was fabricated into 50 mm × 50 mm × 30 mm samples for uniaxial compression test (Fig. 4a). The sample geometry allows accurate measurement of strain, and is considered a fair simplification of the lowermost three-layers. The tests started at 20 min after water addition, as it is assumed that 20 min is a reasonable estimate for start time of printing, considering the time required for material preparation and transport. The loading rate depends on the specific printing process simulated. During the process of 3DP, the vertical buildup rate of the structure is determined by the ratio of the nozzle travelling speed to the length of print path, and is constant for most cases, while the rate of stress accumulation is associated with the buildup rate through layer thickness. For instance, the structure buildup rate is 3 layers/min for a 0.5 m long straight wall printed at a nozzle travelling speed of 1.5 m/min, and the corresponding uniaxial loading rate is thus 1.5 N/min. Similarly, for a 10 layers/min buildup rate, the loading rate is approximately 5 N/min. The loading paths under different printing parameters are shown in Fig. 4b.

An INSTRON 5969 testing machine with a 50 kN loading cell was

Table 2
Properties of PVA fiber.

Length (mm)	Fiber diameter (μm)	Young's modulus (GPa)	Density (kg/m^3)	Surface oil content (wt. %)	Elongation (%)	Nominal Strength (MPa)
8	39	42.8	1300	1.2	6.0	1600

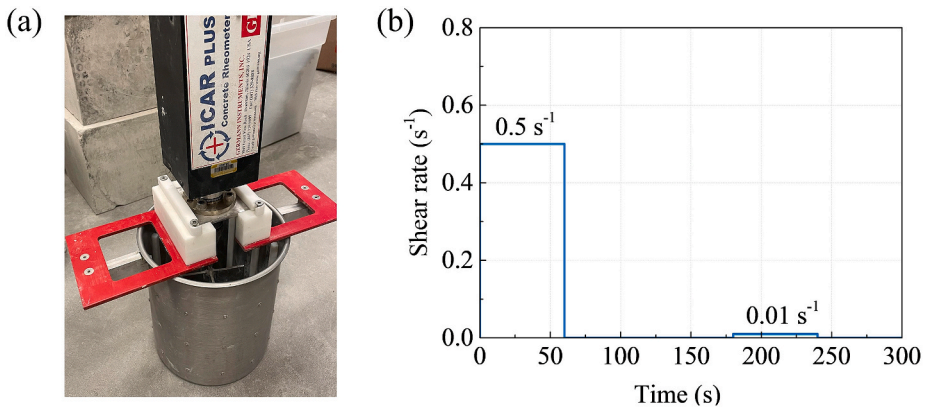

Fig. 3. (a) Test apparatus and (b) test protocol of constant shear rate test.

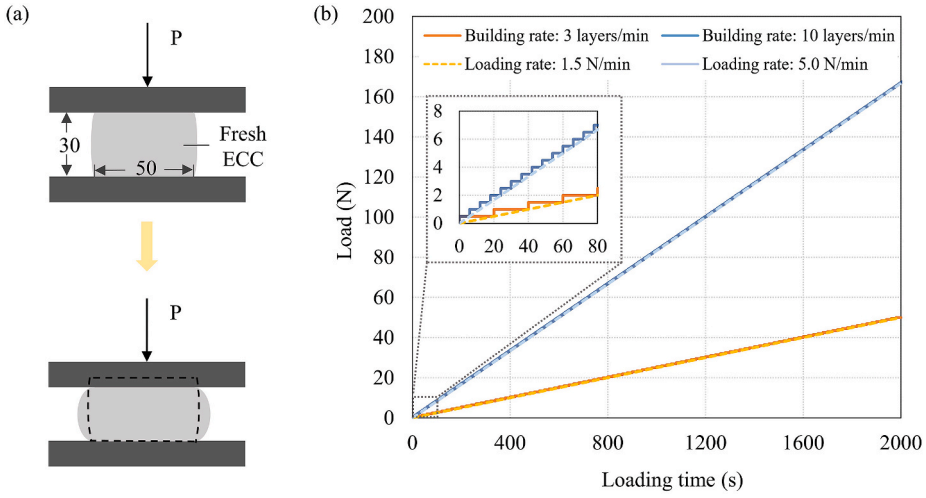

Fig. 4. (a) Test setup (Unit: mm) and (b) loading paths of incremental loading test.

adopted for loading. Lubricant was applied to both loading plates before tests to alleviate the influence of friction. In this test, the geometrical changes of the sample were captured by a high-resolution camera and the strain was analyzed by ImageJ software. Material-scale failure is hereafter defined as fracture onset on the surface or the vertical strain of the sample reaching 40%.

2.5. Green strength test

3D printing is a time-sensitive process. During printing, the components inside the material undergo interactive reactions and property evolution. The hydration process continuously increases the strength and stiffness of the material over time, reducing its fluidity and enhancing the bearing capacity. At the same time, the external load conditions are also changing over time. The deposited material needs to withstand the gravity-induced load exerted by the accumulation of the upper material. These two processes, both progressing with time, are running simultaneously and competing with each other. If and when the bearing capacity of the material is reached and exceeded by external pressure, material failure will occur, which may lead to instability of the underlying layer and further result in overall failure of the structure. To predict the timing of material failure, it is critical to quantify the time dependent loading process and the green property development, and to seek their intersection.

Green strength is an important indicator of material capacity, reflecting mechanical behavior of the material at a certain age. For a time-dependent process like 3DP, material behavior in a single time point is inadequate in depicting and predicting its mechanical response. Hence the green strength time-evolution should be quantified. In this case, fresh ECC specimens of 50 mm × 50 mm × 100 mm were fabricated and loaded under compression at the age of 20–100 min with an interval of 20 min (Fig. 5a). The loading rate was kept at 8 mm/min to ensure tests completed within an average duration of 6 min to minimize the influence of strength development during the test. Before loading, the surface of the specimen was sprayed with random black and white

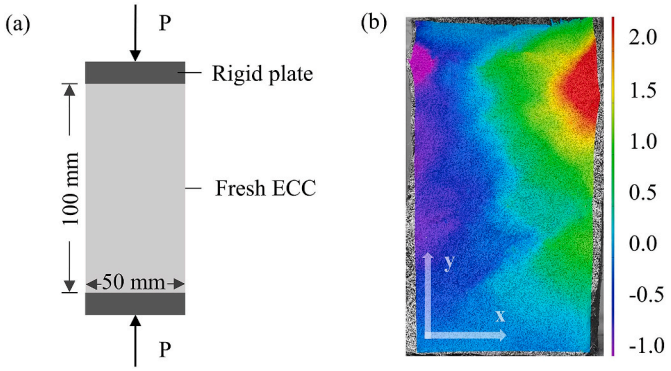

Fig. 5. (a) Test setup of green strength test and (b) displacement field in x-direction when axial strain is at 10% (Unit: mm). (For interpretation of the references to colour in this figure legend, the reader is referred to the Web version of this article.)

speckles to form a unique pattern. Changes in the image patterns during loading were recorded, and processed with Vic-2D software. The strain and displacement distribution could then be calculated and analyzed (Fig. 5b).

3. Results and discussions

3.1. Material scale

3.1.1. Static yield stress evolution

The static yield stress growth of fresh ECC from 20 min to 60 min is summarized in Fig. 6. Beyond 60 min, data is unavailable since the material became stiffer and raised the risk of reaching the torque limit of the testing apparatus. Previous literatures have reported a wide range of initial static yield stress, i.e., from a few hundreds to thousands Pascal, for printable mixtures without fiber. The discrepancy mainly stems from different material status and testing protocols. Commonly, static yield stress within 20 min after water addition is below 5 kPa [16,27,32,36,39,49]. Nonetheless, the yield stress of printable ECC reached approximately 6 kPa at 20 min age, and kept growing at a structuration rate (A_{thix}) of 122 Pa/min. Compared with printable cementitious materials without fiber, the high initial yield stress of ECC offers robust buildability and protects the material from plastic material failure.

It is widely acknowledged that fiber addition promotes the plastic viscosity and the yield stress of fresh cementitious materials within a certain range of dosage [50–53]. Fibers generally increase the surface area that needs to be wetted, thereby reducing the amount of free water to lubricate cement particles [54]. This is especially the case for synthetic fibers, e.g., PVA fibers, due to their low density and large amount. Besides, the intertwining of fibers may also promote resistance to flow and elevate yield stress [55]. The resulting high yield stress poses challenge to the pumping and extruding during 3D printing, yet is favorable to the rapid build-up of structure, since the mechanical capacity of the material is enhanced. This desirable resistance of printable ECC is also confirmed by the incremental loading tests in the later section, and distinguishes printable ECC from conventional mortars and pastes.

3.1.2. Incremental loading

The mechanical response of fresh ECC in the incremental loading tests is shown in Fig. 7. As the tests were performed at different loading rates, the time scales represented by the two curves are different. The rate of material property evolution can be considered to be identical regardless of the loading path. However, for the 1.5 N/min loading, the slow rise in stress allows more time for the material to develop

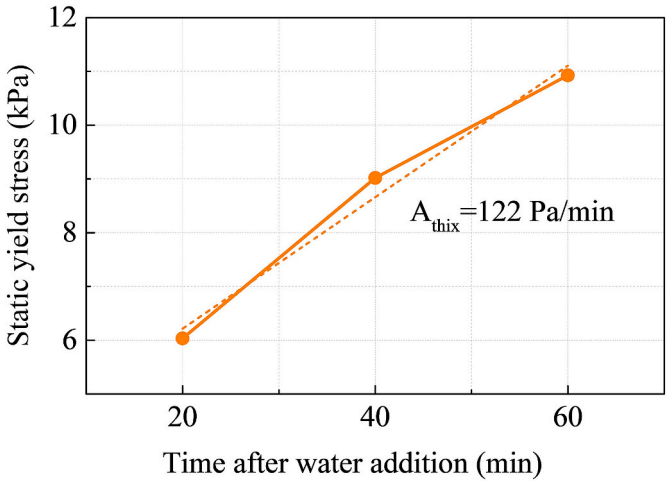

Fig. 6. Static yield stress evolution of fresh printable ECC.

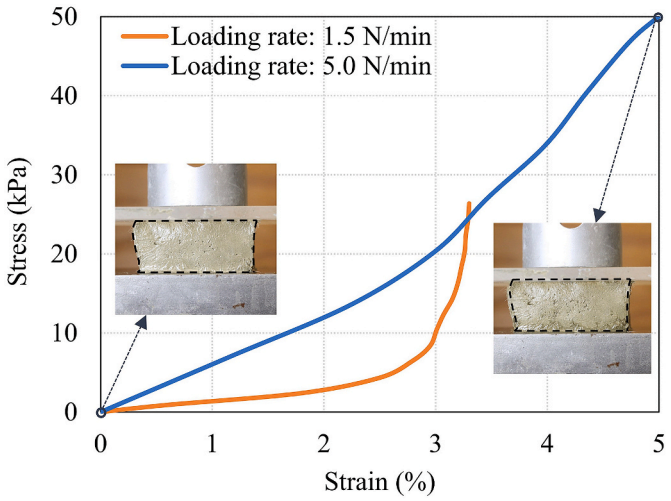

Fig. 7. Mechanical response of fresh printable ECC in incremental loading tests.

resistance. The rate of strain growth slowed down significantly when the strain developed to approximately 3%, at which point the test had been in progress for 16 min. While for a more rapid loading at 5 N/min, 3% strain was reached within 10 min. At 25 min after test initiation, the sample exhibited a vertical strain of 5%, and the corresponding compressive stress reached 50 kPa which approximates 250 layers (2.5 m) of material stacked on the sample.

Despite the relatively rapid buildup rate (10 layers/min) simulated, the printable ECC material experienced only 5% vertical strain in the test, and free of surface fracture, that is, the material showed no sign of failure. The reason why ECC material is effective against material-scale failure lies in the higher growth rate of resistance compared with the external stress buildup. In the next section, the initial bearing capacity of the material (at 20 min after water addition) is also found sufficient to withstand certain external loads. Therefore, both the high initial strength and the fast development of material capacity make printable ECC less vulnerable to material-scale failure.

3.1.3. Green strength development

Fig. 8a plots the tested compressive stress-strain relationships from 20 min to 100 min after water addition. At all ages, stress increased approximately linearly with strain at the beginning stage of loading. After the strain level exceeded 15%, samples with younger ages (less than 60 min after water addition) maintained an approximate linear mechanical response, whilst the samples with a slightly older age (greater than or equal to 60 min) showed a gradual increase in stiffness. As the strain level went beyond 20%, shallow wrinkles and fine cracks began to appear on the surface. Further, when the strain exceeded 35%, the fresh material lost its dimensional stability, and was observed to present undesired fracture on the surface.

Stress data at the 10%, 20% and 30% strain level are extracted, plotted and connected separately in Fig. 8b to create stress contours. Meanwhile, the compressive stress accumulated during printing is also mapped in the same figure. The slope of the stress accumulation line is determined by the structure buildup rate, i.e., ratio of printing speed to length of printing path. Two different structures were taken as examples - a 0.5 m long straight wall and a hollow cylinder with a diameter of 0.3 m, both printed at 1.2 m/min. The printing speed is identical to that adopted in actual printing and is determined based on the on-site material status and the synchronization among different devices.

It is found that the only intersection between the stress contours and the stress accumulation line is at the 10% strain level, which means, theoretically, the maximum strain the material could develop is slightly above 10%. According to the previous definition, 10% strain in material is not capable of inducing material failure. This result verifies the

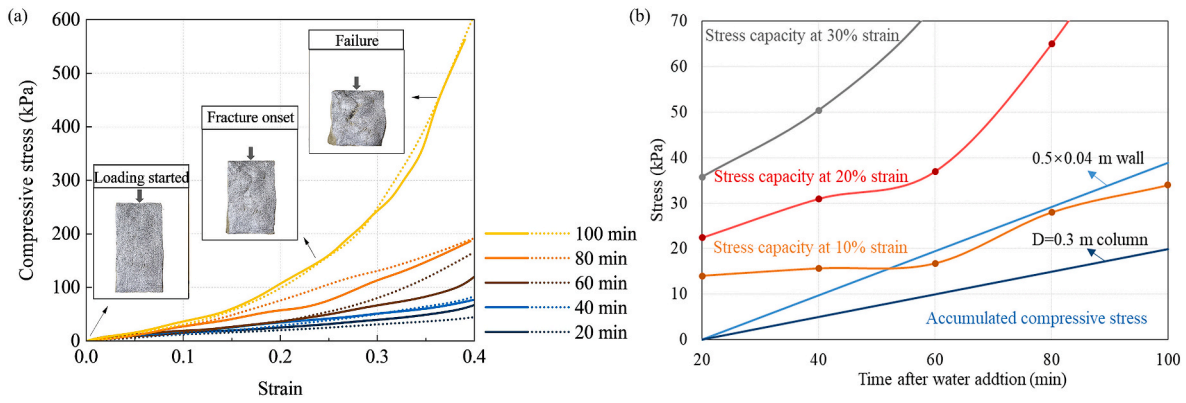

Fig. 8. (a) Green stress capacity of printable ECC evolving with time and (b) its comparison with accumulated compressive stress. (For interpretation of the references to colour in this figure legend, the reader is referred to the Web version of this article.)

preliminary conclusion obtained in Section 3.1.1, that for printable ECC, the probability of material-scale damage is insignificant.

3.1.4. Time-dependent strain-stress model

Although the reliability of printable ECC at the material scale is confirmed, the mechanical response and geometric changes of the material during printing are still of interest. On the premise that no structural collapse is induced by material failure, the emphasis of buildability evaluation should be put on the shape retention ability of the filaments. The geometric change in filament shape under load is of vital significance to the printed structure - the accumulation of deformation in each layer will ultimately affect the overall strain and structural stability of the finished product.

To evaluate the mechanical response of materials in this case, two key issues need to be addressed: (1) As aforementioned, the properties of the material and the external accumulated stress are two time-varying indices that are independent of each other. It is necessary to seek the law of their independent development, and further link the two together through the 3D printing process. (2) The 3D printed structure is created by stacking multiple layers of filaments, and the gravity-induced stress borne by each layer of material is nonlinear. In this case, the overall assessment of the structure needs to cover the individual behaviors of all

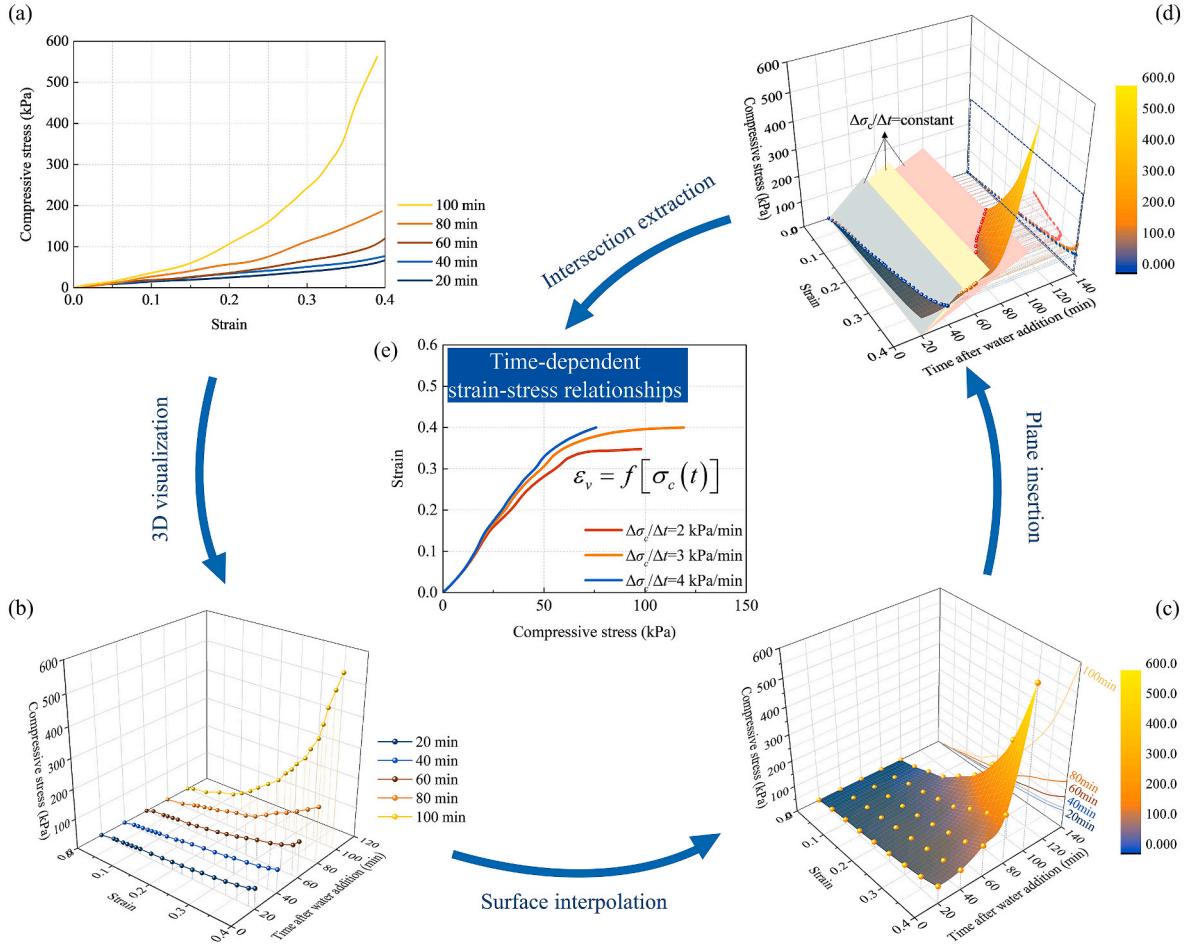

Fig. 9. Methodology for developing the time-dependent strain-stress model.

filaments.

To address the first issue, a time-dependent mechanical model needs to be established. The time-dependent mechanical properties of the material have been obtained from green strength tests (Fig. 9a). The next step is to visualize the time-related information implicit in the data. For this purpose, a 3D coordinate is created with strain (x-axis), time after water addition (y-axis) and stress (z-axis) being the axes. The original 2D stress-strain curves are marked in the new 3D coordinate, arranged in chronological order along the y-axis (Fig. 9b). Since the current data only represent the material behavior at discrete ages, the behavior on a continuous timeline needs to be reasonably inferred. Through interpolation, a continuous and smooth 3D surface is constructed, representing the time-dependent mechanical behavior of the deposited ECC material (Fig. 9c).

Regarding structure buildup, a constant buildup rate (as is the case for the vast majority of printings) is assumed, the ratio of compressive stress growth to time development is thus invariable, denoted as $\Delta\sigma_c/\Delta t$. In Fig. 8b, this ratio represents the slope of the 2D stress accumulation line; while in Fig. 9d, it is the slope of the inclined plane in the 3D coordinate, since the pre-set printing program will not be disturbed by material property, i.e., the ratio is independent of the material strain represented by the x-axis. Different printing settings (including varying nozzle movement speeds, contour lengths, layer thicknesses, etc.) will generate specific buildup rates, which correspond to the inclined planes with varying slopes in the 3D coordinate system. Three inclined planes are inserted as examples in Fig. 9d, which correspond to three different $\Delta\sigma_c/\Delta t$ ratios, i.e., 2, 3, 4 kPa/min. It can be observed in Fig. 9d that each plane has an intersection line with the generated surface. These intersection lines describe the early compressive stress-strain response of fresh ECC material at the specified buildup rates. By projecting the intersection line onto the stress-strain plane (x-z plane), a new strain-stress model is thus established (Fig. 9e). It is worth noting that the time variable is no longer present in this model, however, the evolution of mechanical behavior induced by time progress is implicit in this 2D model. That is, the derived time-dependent strain-stress relationship is based on a certain time path and loading path, but the two variables of time and buildup rate are excluded from the simplified expression through the proposed modeling approach.

The reason why the proposed model is a strain-stress model but not the other way around is that the focus is put on the strain response of the material while the stress progresses according to a known path pre-set by the printing program. In addition, the intersection line generated by the 2 kPa/min plane in Fig. 9d contains a descending segment of the strain-stress curve. However, in consideration of material behavior, the descending branch does not have any practical and effective meaning. At the strain peak, ECC material has developed sufficient resistance to prevent further substantial deformation. As the stress further increases, the strain should therefore generate a plateau rather than a drop. With this consideration, the proposed strain-stress model excludes the descending segment.

The time-dependent strain-stress model proposed above provides the basis for material scale analysis, yet it is still at the scale of a single filament. Hence, further processing is required to integrate the behavior of multiple filament units into the behavior of the printed structure. In the strain-stress model, the material behavior in different layers is represented by discrete data points on the continuous curve. For simplification, the coordinate where the model sits is scaled as shown in Fig. 10a. The abscissa is modified from stress to the number of layers, which are linearly proportional with each other (Eq. (3)).

$$\sigma_H = \rho g H = N \cdot \Delta\sigma_0 = N \cdot \rho g h_0 \tag{3}$$

where N is the total number of layers for a printed structure with height H.

For a printed structure with N layers and height H, the bottom material corresponds to the strain $\varepsilon_{N\text{-}1}$ in Fig. 10a. The vertical deformation of this layer can be determined by $\varepsilon_{N\text{-}1}$ multiplied by h_0. Similarly, the vertical deformation of the overall structure can be written as the sum of each layer's deformations and thus can be approximated by the integral of the curve from 0 to N (Eq. (4)).

$$\Delta H = (\varepsilon_{N-1} + \varepsilon_{N-2} + \ldots + \varepsilon_1) h_0 = \sum_{n=1}^{N-1} \varepsilon_n h_0 \approx h_0 \int_0^N g(n) dn \tag{4}$$

where ε_i represents the vertical strain of the i th layer, $g(n)$ is the vertical strain as a function of layer number n.

Furthermore, with the abscissa reverted back to strain, the relationship between vertical deformation and the integral of strain-stress model is therefore obtained (Eq. (5)), as illustrated in Fig. 10b.

$$\Delta H \approx h_0 \int_0^{\sigma_H} f(\sigma_c) \cdot \frac{1}{\Delta\sigma_0} \cdot d(\Delta\sigma_0 \cdot n) = \frac{1}{\rho g} \int_0^{\sigma_H} f(\sigma_c) d\sigma_c \tag{5}$$

where f (σ_c) is the vertical strain as a function of accumulated compressive stress, σ_H is the accumulated stress on the bottom material.

To validate the proposed model, a straight wall with a length of 0.5 m was printed (Fig. 11b). The wall thickness on the horizontal plane is the width of a single filament, which is approximately 40 mm. Before the structure underwent self-buckling, 22 layers were stacked and a total height of 217 mm was observed. According to the printing settings of 10 mm layer thickness, the measured wall height reflected a vertical deformation of approximately 3 mm.

In this test, the printing nozzle traveled at a speed of 1.2 m/min, indicating a vertical stress growth rate of 0.47 kPa/min. An inclined

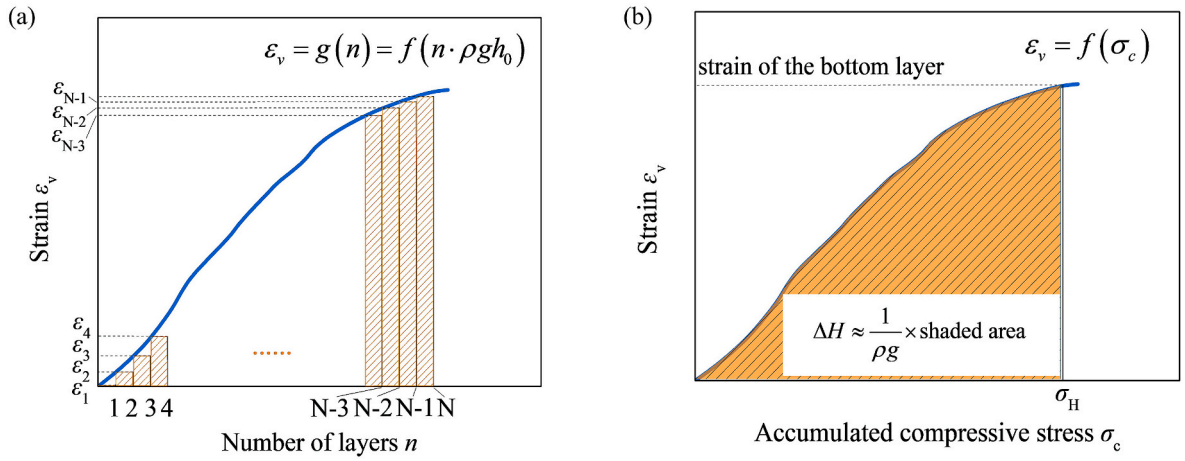

Fig. 10. Derivation of accumulated vertical deformation of a multi-layered printed element.

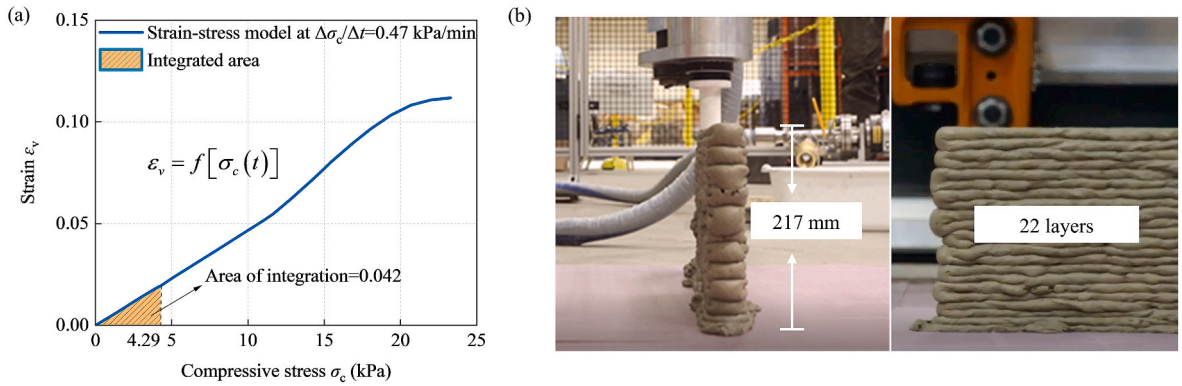

Fig. 11. (a) Model prediction and (b) experimental verification of accumulated deformation of 3D printed structure.

plane corresponding to this slope is inserted into the 3D coordinate system in Fig. 9c to obtain the intersection projection, that is, the time-dependent strain-stress model under this specific structure buildup rate (Fig. 11a). The structural height of 22 layers implies a cumulative compressive stress σ_H of 4.29 kPa. Therefore, the strain-stress function is integrated from 0 to 4.29 kPa to obtain the prediction result of 2.2 mm. Hence, the predicted deformation correlates reasonably with the 3 mm experimental result.

In this proposed model, 3DP-ECC is emphasized as the printing ink of interest. Nonetheless, the approach is valuable as a universal modeling methodology. This means that the underlying logic of establishing the time-dependent mechanical model as well as predicting structure deformation from laboratory material testing is also applicable to other types of 3D printed cementitious materials.

This model can demonstrate practical meanings in multiple scenarios: (1) by characterizing the material properties in the laboratory, it is possible to make an ex ante prediction of the structural deformation, which gives researchers and engineers the freedom to improve and optimize geometric control of the to-be-printed structure from the initial stage of material formulation; (2) the prediction given by the model can be used to modify and adjust the nozzle standoff distance during printing to avoid the structural instability problem caused by structure subsidence and constant nozzle elevation; (3) the time-dependent stress-strain constitutive relations could be incorporated into finite element analysis, providing theoretical basis and necessary material parameters for the early-age mechanical behavior analysis of the printed structure.

It is worth noting that further improvements can be applied to the model. First, the geometric dimension of the specimens in green strength tests was designed for compression tests, and lateral support provided by adjacent material during printing is not taken into consideration for simplification. The unconfined uniaxial compressive test does not necessarily simulate the material dimensions and stress states in actual printing. Therefore, with the modeling approach not affected, the material characterization method can be modified to further approximate the actual stress state of the material in 3D printed structures. For example, confined uniaxial compressive tests with stacking layers [38] may be considered. In addition, this model does not take into account the influence of vertical stress applied by nozzle, which may be a concern for the cases where deposited filament is pressed by a lowered nozzle (e.g., using a down-flow circular nozzle with a lowered nozzle standoff distance). Further modification of the model prediction is needed when such printing setup is applied.

3.2. Structural scale

At the material scale, it has been elucidated that the excellent strength capacity of fresh ECC material effectively prevents collapse caused by material failure, indicating that for most cases, failure originated from structural instability will be the primary failure mode of 3DP-ECC.

Generally, self-buckling of a slender structure under its self-weight is controlled by its material property, structural form and dimensions. As in Eq. (1), the critical height of a slender structure H_c is affected by material density ρ, stiffness E, second moment of inertia I and horizontal cross-sectional area A. Structural stability is difficult to be maintained under the self-weight when the height of the structure exceeds this threshold. This evaluation criterion has been suggested by Roussel [8] as a critical state for elastic buckling failure for 3DP structures. For conventional cast concrete structures, all the above parameters are fixed time-invariant values for a specific structure; for 3DP, however, the stiffness E is no longer a constant but a time-varying variable. The critical height of a printed structure at self-buckling is thus a function of time (Eq. (6)) and can be predicted by characterizing the stiffness evolution of the material.

$$H_c(t) \approx \left[\frac{8E(t)I}{\rho g A}\right]^{1/3} \tag{6}$$

To verify the above statement, two structures were designed and printed at 1.2 m/min – a 0.5 m straight wall (Fig. 12a) and a 0.3 m diameter hollow cylinder (Fig. 12b). For the straight wall, the critical height function can be simplified as in Eq. (7) by plugging in the geometrical parameters using the second moment of area I for a rectangular cross-section.

$$H_c(t) \approx \left[\frac{2E(t)\delta^2}{3\rho g}\right]^{1/3} \tag{7}$$

where δ is the thickness of the wall.

Stiffness evolution of the material can be extracted from the green strength test results (Fig. 13a). Generally, the elastic modulus of a material is estimated from the linear elastic segment of the compressive stress-strain curve. According to ASTM C469/C469M − 14 [56], the modulus of elasticity is considered to be the tangential modulus before stress reaches 40% of the ultimate load. However, early-age ECC maintained a continuous increase in stress during compression, with no peak present. The approximately linear segments before 10% strain are adopted to derive the material stiffness at different ages [34] (Fig. 13b). Assuming a linear development of stiffness (unit: kPa) with time (unit: min), an approximation of stiffness is fitted in Fig. 13c (Eq. (8)).

$$E(t) \approx 2.65 \cdot t + 43 \tag{8}$$

Integrating Eq. (7) and Eq. (8), the $H_c(t)$ function for the straight wall is plotted in Fig. 13d. Under a fixed printing path and speed, structural height elevation as a function of time is also mapped onto the same coordinate. The two functions are found to intersect at $t = 23$ min. At this time, the printed structural height catches up and exceeds the maximum allowable height that the material stiffness can support, leading to self-buckling of the structure post this point. Corresponding to

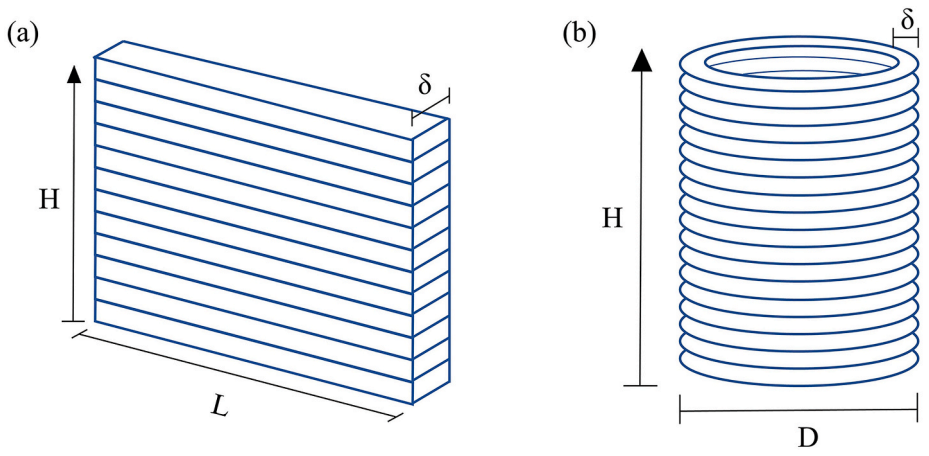

Fig. 12. Schematic configuration of printed (a) straight wall and (b) hollow cylinder.

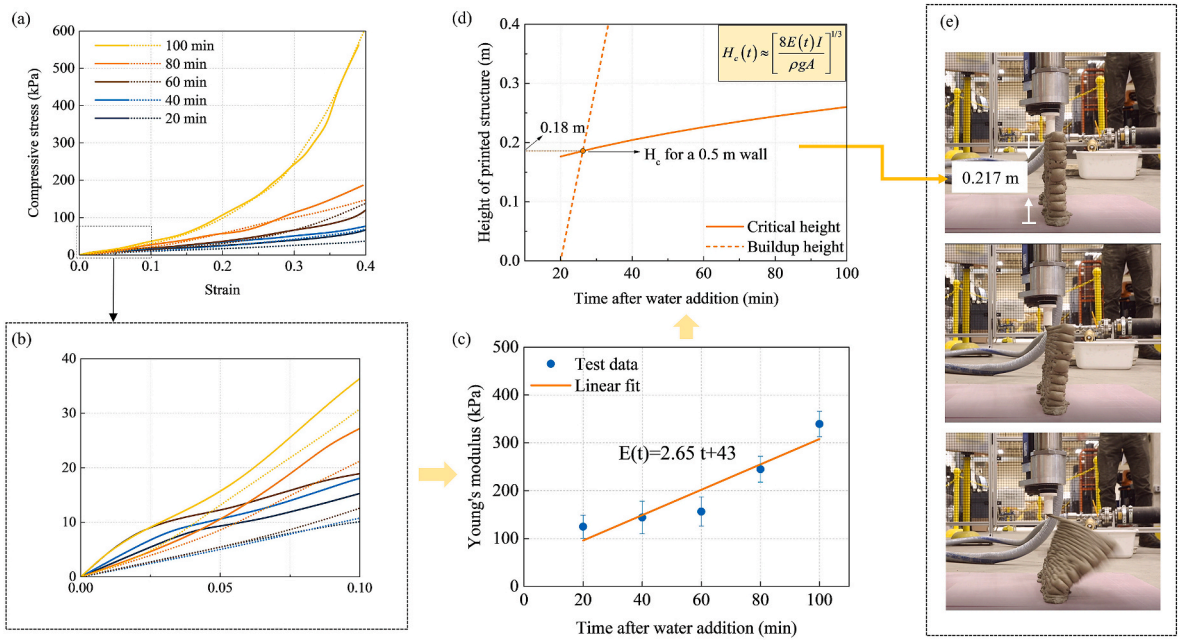

Fig. 13. Methodology and validation for predicting self-buckling of printed ECC element.

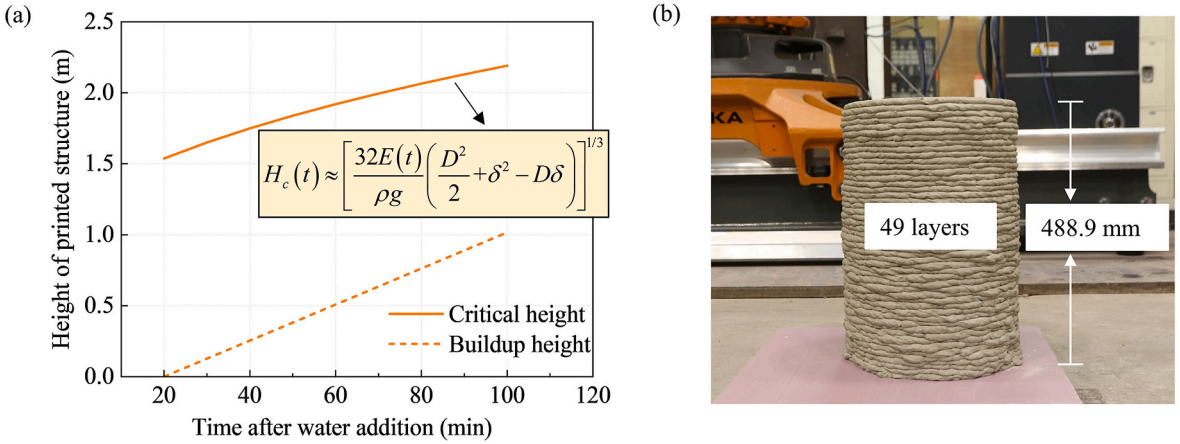

Fig. 14. (a) Model prediction and (b) experimental verification of stability of a 3D printed hollow cylindrical column.

the intersection point, a structural failure height of 0.18 m is predicted. While in actual printing, the straight wall collapsed at a height of 0.217 m, as shown in Fig. 13e, which is in reasonable agreement with the prediction.

Similarly, for the hollow cylinder in Fig. 12b, the critical height and buildup height can be derived as functions of time (Fig. 14a) using the appropriate I for a circular cross-section. Unlike the previous case of straight wall, the two functions do not intersect within 100 min, meaning that structural self-buckling will not occur within this time range. Two primary reasons for the difference lie in: (1) under the same nozzle travel speed, the printing path length of the cylinder (0.942 m) is considerably longer than that of the straight wall (0.5 m), leading to slower structure height elevation; (2) the inherent geometric stability (represented by larger I/A value in Eq. (6)) of the cylindrical structure outperforms that of the straight wall. Self-buckling is thus less likely to occur. The cylinder was eventually printed to 49 layers and reached a height of 488.9 mm without any signs of structural instability (Fig. 14b).

From the above analysis, it can be concluded that at the structural scale, critical structural height for self-buckling can be predicted on the basis of material stiffness evolution. Laboratory characterization of materials can provide an assessment of structural stability, which in turn acts as feedback and presents specific and quantitative requirements on material tailoring. Furthermore, based on this evaluation approach, premature self-bucking could be delayed or avoided by proper design of the structural geometry and the buildup rate. The understanding of the properties of printing materials sets clear boundaries for structural design of 3DP.

4. Conclusions

The present study developed a consistent and quantitative evaluation approach for buildability of 3DP-ECC, covering both the material and the structural scale. Instead of focusing only on material properties at certain ages, a methodology is proposed that recognizes evolving material behavior on a continuous timeline and that incorporates the information of designed printing. The influence of time progress is elaborated and embodied in the proposed time-dependent model.

Through experimental investigation and theoretical analysis, the following conclusions can be drawn:

1. At the material scale, printable ECC material develops satisfying resistance to the accumulated vertical stress from upper layers at the early age. Constant shear rate test, incremental loading test and green strength test demonstrated that the risk of material failure is low, at least for the material composition and processing approach used in the present research.
2. Although material failure is not likely, geometric changes of the printed structure and mechanical response of the fresh material are of interest. A time-dependent strain-stress model of fresh ECC was proposed based on green strength development of the material. The proposed model makes reasonable prediction of structural deformation during deposition and lays the foundation for mechanical analysis of fresh extruded structure.
3. At the structural scale, the critical height for self-buckling during printing can be predicted on the basis of stiffness evolution. Based on the evaluation approach, premature self-bucking could be avoided by proper design of the structural geometry and the buildup rate (printing parameters), for a given material behavior evolution.
4. The time-dependent fresh properties of printable material and the design parameters of 3DP (including structure design and printing parameters) are linked through time-related analyses. Buildability evaluations based on laboratory characterization of materials at both material and structural scales are therefore enabled.
5. While the experimental work in the research reported here focuses on ECC material, the methodology proposed for buildability evaluation is applicable to 3D printing of concrete material in general. Hence this research contributes to the development of 3D printing of large scale civil and architectural structures.

Authorship contribution statement

Wen Zhou: Conceptualization, Methodology, Investigation, Validation, Writing - Original Draft.

Wes McGee: Investigation, Writing - review & editing.

He Zhu: Investigation, Writing - review & editing.

H. Süleyman Gökçe: Investigation.

Victor C. Li: Conceptualization, Methodology, Supervision, Writing - review & editing.

Declaration of competing interest

The authors declare that they have no known competing financial interests or personal relationships that could have appeared to influence the work reported in this paper.

Data availability

Data will be made available on request.

Acknowledgments

Financial support of this research is provided by the University of Michigan MCubed 3 Program, the Center for Low Carbon Built Environment (CLCBE) and the James R. Rice Distinguished University Professorship. The Department of Civil and Environmental Engineering at the University of Michigan provides financial support for the robotic 3DP equipment. W. Zhou is supported by a University of Michigan fellowship for graduate studies. H. Süleyman Gökçe would like to acknowledge the postdoctoral research fellowship supported by The Scientific and Technological Research Council of Turkey (TUBITAK).

References

[1] G. De Schutter, K. Lesage, V. Mechtcherine, V.N. Nerella, G. Habert, I. Agusti-Juan, Vision of 3D printing with concrete — technical, economic and environmental potentials, Cement. Concrete. Res. 112 (2018) 25–36.
[2] M.K. Mohan, A.V. Rahul, G. De Schutter, K. Van Tittelboom, Extrusion-based concrete 3D printing from a material perspective: a state-of-the-art review, Cement Concr. Compos. 115 (2021), 103855.
[3] R.A. Buswell, W.R. Leal De Silva, S.Z. Jones, J. Dirrenberger, 3D printing using concrete extrusion: a roadmap for research, Cement. Concrete. Res. 112 (2018) 37–49.
[4] G. Ma, R. Buswell, W.R. Leal Da Silva, L. Wang, J. Xu, S.Z. Jones, Technology readiness: a global snapshot of 3D concrete printing and the frontiers for development, Cement. Concrete. Res. 156 (2022), 106774.
[5] I. Agustí-Juan, G. Habert, Environmental design guidelines for digital fabrication, J. Clean. Prod. 142 (2017) 2780–2791.
[6] I. Agustí-Juan, F. Müller, N. Hack, T. Wangler, G. Habert, Potential benefits of digital fabrication for complex structures: environmental assessment of a robotically fabricated concrete wall, J. Clean. Prod. 154 (2017) 330–340.
[7] B. Lu, Y. Weng, M. Li, Y. Qian, K.F. Leong, M.J. Tan, S. Qian, A systematical review of 3D printable cementitious materials, Constr. Build. Mater. 207 (2019) 477–490.
[8] N. Roussel, Rheological requirements for printable concretes, Cement. Concrete. Res. 112 (2018) 76–85.
[9] L. Reiter, T. Wangler, N. Roussel, R.J. Flatt, The role of early age structural build-up in digital fabrication with concrete, Cement. Concrete. Res. 112 (2018) 86–95.
[10] M.S. Khan, F. Sanchez, H. Zhou, 3-D printing of concrete: beyond horizons, Cement. Concrete. Res. 133 (2020), 106070.
[11] M. Amran, H.S. Abdelgader, A.M. Onaizi, R. Fediuk, T. Ozbakkaloglu, R.S. M. Rashid, G. Muralih, 3D-printable alkali-activated concretes for building applications: a critical review, Constr. Build. Mater. 319 (2022), 126126.
[12] Y. Zhang, Y. Zhang, G. Liu, Y. Yang, M. Wu, B. Pang, Fresh properties of a novel 3D printing concrete ink, Constr. Build. Mater. 174 (2018) 263–271.
[13] S. Muthukrishnan, S. Ramakrishnan, J. Sanjayan, Technologies for improving buildability in 3D concrete printing, Cement Concr. Compos. 122 (2021), 104144.
[14] T. Wangler, N. Roussel, F.P. Bos, T.A.M. Salet, R.J. Flatt, Digital concrete: a review, Cement. Concrete. Res. 123 (2019), 105780.
[15] N. Roussel, A thixotropy model for fresh fluid concretes: theory, validation and applications, Cement. Concrete. Res. 36 (2006) 1797–1806.
[16] A. Perrot, D. Rangeard, A. Pierre, Structural built-up of cement-based materials used for 3D-printing extrusion techniques, Mater. Struct. 49 (2016) 1213–1220.

[17] R.J.M. Wolfs, F.P. Bos, T.A.M. Salet, Early age mechanical behaviour of 3D printed concrete: numerical modelling and experimental testing, Cement. Concrete. Res. 106 (2018) 103–116.
[18] A.V. Rahul, M.K. Mohan, G. De Schutter, K. Van Tittelboom, 3D printable concrete with natural and recycled coarse aggregates: rheological, mechanical and shrinkage behaviour, Cement Concr. Compos. 125 (2022), 104311.
[19] V.N. Nerella, M. Krause, V. Mechtcherine, Direct printing test for buildability of 3D-printable concrete considering economic viability, Automat. Constr. 109 (2020), 102986.
[20] A.S.J. Suiker, Mechanical performance of wall structures in 3D printing processes: theory, design tools and experiments, Int. J. Mech. Sci. 137 (2018) 145–170.
[21] T.T. Le, S.A. Austin, S. Lim, R.A. Buswell, A.G.F. Gibb, T. Thorpe, Mix design and fresh properties for high-performance printing concrete, Mater. Struct. 45 (2012) 1221–1232.
[22] A. Kazemian, X. Yuan, E. Cochran, B. Khoshnevis, Cementitious materials for construction-scale 3D printing: laboratory testing of fresh printing mixture, Constr. Build. Mater. 145 (2017) 639–647.
[23] B. Panda, M.J. Tan, Rheological behavior of high volume fly ash mixtures containing micro silica for digital construction application, Mater. Lett. 237 (2019) 348–351.
[24] Y. Weng, M. Li, M.J. Tan, S. Qian, Design 3D printing cementitious materials via Fuller Thompson theory and Marson-Percy model, Constr. Build. Mater. 163 (2018) 600–610.
[25] C. Joh, J. Lee, T.Q. Bui, J. Park, I. Yang, Buildability and mechanical properties of 3D printed concrete, Materials 13 (2020) 4919.
[26] S. Ahmed, S. Yehia, Evaluation of workability and structuration rate of locally developed 3D printing concrete using conventional methods, Materials 15 (2022) 1243.
[27] Q. Yuan, Z. Li, D. Zhou, T. Huang, H. Huang, D. Jiao, C. Shi, A feasible method for measuring the buildability of fresh 3D printing mortar, Constr. Build. Mater. 227 (2019), 116600.
[28] Y. Chen, S. Chaves Figueiredo, Z. Li, Z. Chang, K. Jansen, O. Çopuroğlu, E. Schlangen, Improving printability of limestone-calcined clay-based cementitious materials by using viscosity-modifying admixture, Cement. Concrete. Res. 132 (2020), 106040.
[29] Q. Liu, Q. Jiang, M. Huang, J. Xin, P. Chen, S. Wu, Modifying effect of anionic polyacrylamide dose for cement-based 3DP materials: printability and mechanical performance tests, Constr. Build. Mater. 330 (2022), 127156.
[30] L. Casagrande, L. Esposito, C. Menna, D. Asprone, F. Auricchio, Effect of testing procedures on buildability properties of 3D-printable concrete, Constr. Build. Mater. 245 (2020), 118286.
[31] R.J.M. Wolfs, F.P. Bos, T.A.M. Salet, Triaxial compression testing on early age concrete for numerical analysis of 3D concrete printing, Cement Concr. Compos. 104 (2019), 103344.
[32] B. Panda, J.H. Lim, M.J. Tan, Mechanical properties and deformation behaviour of early age concrete in the context of digital construction, Compos. B Eng. 165 (2019) 563–571.
[33] Y. Wang, Y. Jiang, T. Pan, K. Yin, The synergistic effect of ester-ether copolymerization thixo-tropic superplasticizer and nano-clay on the buildability of 3D printable cementitious materials, Materials 14 (2021) 4622.
[34] A. Tripathi, S.A.O. Nair, N. Neithalath, A comprehensive analysis of buildability of 3D-printed concrete and the use of bi-linear stress-strain criterion-based failure curves towards their prediction, Cement Concr. Compos. 128 (2022), 104424.
[35] B. Zhu, B. Nematollahi, J. Pan, Y. Zhang, Z. Zhou, Y. Zhang, 3D concrete printing of permanent formwork for concrete column construction, Cement Concr. Compos. 121 (2021), 104039.
[36] R. Jayathilakage, P. Rajeev, J.G. Sanjayan, Yield stress criteria to assess the buildability of 3D concrete printing, Constr. Build. Mater. 240 (2020), 117989.
[37] J. Kruger, S. Zeranka, G. van Zijl, 3D concrete printing: a lower bound analytical model for buildability performance quantification, Automat. Constr. 106 (2019), 102904.
[38] I. Ivanova, E. Ivaniuk, S. Bisetti, V.N. Nerella, V. Mechtcherine, Comparison between methods for indirect assessment of buildability in fresh 3D printed mortar and concrete, Cement. Concrete. Res. 156 (2022), 106764.
[39] M. Tramontin Souza, I. Maia Ferreira, E. Guzi De Moraes, L. Senff, S. Arcaro, J. R. Castro Pessôa, M.J. Ribeiro, A.P. Novaes De Oliveira, Role of chemical admixtures on 3D printed Portland cement: assessing rheology and buildability, Constr. Build. Mater. 314 (2022), 125666.
[40] G. Ma, Z. Li, L. Wang, Printable properties of cementitious material containing copper tailings for extrusion based 3D printing, Constr. Build. Mater. 162 (2018) 613–627.
[41] V.C. Li, Engineered Cementitious Composites (ECC), first ed., Springer, Berlin, Germany, 2019.
[42] V.C. Li, F.P. Bos, K. Yu, W. McGee, T.Y. Ng, S.C. Figueiredo, K. Nefs, V. Mechtcherine, V.N. Nerella, J. Pan, G.P.A.G. van Zijl, P.J. Kruger, On the emergence of 3D printable engineered, strain hardening cementitious composites (ECC/SHCC), Cement. Concrete. Res. 132 (2020), 106038.
[43] H. Zhu, K. Yu, W. McGee, T.Y. Ng, V.C. Li, Limestone calcined clay cement for three-dimensional- printed engineered cementitious composites, ACI Mater. J. 118 (2021).
[44] K. Yu, W. McGee, T.Y. Ng, H. Zhu, V.C. Li, 3D-printable engineered cementitious composites (3DP-ECC): fresh and hardened properties, Cement. Concrete. Res. 143 (2021), 106388.
[45] S.C. Figueiredo, C.R. Rodríguez, Z.Y. Ahmed, D.H. Bos, Y. Xu, T.M. Salet, O. Çopuroğlu, E. Schlangen, F.P. Bos, An approach to develop printable strain hardening cementitious composites, Mater. Design. 169 (2019), 107651.
[46] B. Zhu, J. Pan, B. Nematollahi, Z. Zhou, Y. Zhang, J. Sanjayan, Development of 3D printable engineered cementitious composites with ultra-high tensile ductility for digital construction, Mater. Design. 181 (2019), 108088.
[47] H. Ogura, V. Nerella, V. Mechtcherine, Developing and testing of strain-hardening cement-based composites (SHCC) in the context of 3D-printing, Materials 11 (2018) 1375.
[48] A.L. van Overmeir, S.C. Figueiredo, B. Šavija, F.P. Bos, E. Schlangen, Design and analyses of printable strain hardening cementitious composites with optimized particle size distribution, Constr. Build. Mater. 324 (2022), 126411.
[49] C. Matthäus, D. Back, D. Weger, T. Kränkel, J. Scheydt, C. Gehlen, Effect of Cement Type and Limestone Powder Content on Extrudability of Lightweight Concrete, vol. 2020, Second RILEM International Conference on Concrete and Digital Fabrication, DC, 2020, pp. 312–322.
[50] A.S. El-Dieb, M.M.R. Taha, Flow characteristics and acceptance criteria of fiber-reinforced self-compacted concrete (FR-SCC), Constr. Build. Mater. 27 (2012) 585–596.
[51] P.F.G. Banfill, G. Starrs, G. Derruau, W.J. McCarter, T.M. Chrisp, Rheology of low carbon fibre content reinforced cement mortar, Cement Concr. Compos. 28 (2006) 773–780.
[52] W. Wang, A. Shen, Z. Lyu, Z. He, K.T.Q. Nguyen, Fresh and rheological characteristics of fiber reinforced concrete——a review, Constr. Build. Mater. 296 (2021), 123734.
[53] L. Martinie, P. Rossi, N. Roussel, Rheology of fiber reinforced cementitious materials: classification and prediction, Cement. Concrete. Res. 40 (2010) 226–234.
[54] M. Cao, L. Xu, C. Zhang, Rheology, fiber distribution and mechanical properties of calcium carbonate (CaCO3) whisker reinforced cement mortar, Compos. Appl. Sci. Manuf. 90 (2016) 662–669.
[55] S. Jiang, B. Shan, J. Ouyang, W. Zhang, X. Yu, P. Li, B. Han, Rheological properties of cementitious composites with nano/fiber fillers, Constr. Build. Mater. 158 (2018) 786–800.
[56] ASTM C469/C469M, Standard Test Method for Static Modulus of Elasticity and Poisson's Ratio of Concrete in Compression, ASTM International, 2014.